Three-dimensional grain growth in pure iron. Part I. statistics on the grain level

Jin Zhang, Yubin Zhang, Wolfgang Ludwig, David Rowenhorst, Peter W Voorhees, Henning F Poulsen

Three-dimensional grain growth in pure iron. Part I. statistics on the grain level

Jin Zhang[a], Yubin Zhang[b,*], Wolfgang Ludwig[c], David Rowenhorst[d], Peter W. Voorhees[e], Henning F. Poulsen[a,**]

[a] *NEXMAP, Department of Physics, DTU, 2800 Kongens Lyngby, Denmark*
[b] *Department of Mechanical Engineering, DTU, 2800 Kongens Lyngby, Denmark*
[c] *European Synchrotron Radiation Facility, 38043 Grenoble, France*
[d] *Materials Science and Technology Division, The US Naval Research Laboratory, Washington, D.C. 20735, USA*
[e] *Department of Materials Science and Engineering, Northwestern University, Evanston, IL, 60208, USA*

Abstract

Grain evolution in pure iron is determined in three dimensions using diffraction contrast tomography at a synchrotron source. During annealing for 75 minutes at $800°C$, the evolution of initially 1327 grains is quantified as a function of 15 time-steps. A comprehensive statistical analysis is provided based on the equivalent radius, the number of faces and the mean width parameters of the grains. We introduce analytical relations between these parameters, validate them, and discuss their physical meaning. While the sample is fully recrystallized, the growth is found not to be self-similar, as evidenced in changes in the distributions of normalized grain size and number of faces per grain. More importantly, a strong decrease in the slope of the growth rate over the mean width of grain faces is observed, indicating a slowdown of grain growth. The data is used to determine the applicability of the isotropic MacPherson-Srolovitz theory to an anisotropic material such as iron. Geometrical properties that are averaged over the entire grain ensemble are well described by the model, but the properties and evolution of the individual grains exhibit substantial scatter.

Keywords: Diffraction contrast tomography (DCT), Ferrite, Microstructure, X-ray synchrotron radiation, Temporal evolution

1. Introduction

Grain growth is an integral part of the thermal processing of most polycrystalline materials. It is a complicated process, involving crystallographic,

*Corresponding author
**Principal corresponding author
Email addresses: yubz@dtu.dk (Yubin Zhang), hfpo@fysik.dtu.dk (Henning F. Poulsen)

geometrical, and topological changes of the microstructure [1] under various driving forces [2]. The fact that mobilities and grain boundary energies depend on misorientations and boundary plane inclinations [2, 3] further complicates the situation. In the past 70 years, a great variety of grain growth models have been introduced, including analytical theories in 2D [4, 5] and in 3D [6, 7], and simulations using Monte Carlo Potts models [8], vertex models [9, 10], level-set based methods [11, 12], and phase-field methods [13–16]. Generally speaking, these models make the assumption of isotropic energies and mobilities of the interfaces, thus they only directly apply to idealized situations.
As an example, for one class of models, the growth rate of a grain with anisotropic grain boundary mobility M and energy γ is determined from differential geometry and Herring's relation [17]

$$\frac{\mathrm{d}V}{\mathrm{d}t} = -\int_{\Gamma_{\mathrm{face}}} 2M\gamma\mathcal{H} + M\left(\frac{\partial^2\gamma}{\partial n_1^2}\kappa_1 + \frac{\partial^2\gamma}{\partial n_2^2}\kappa_2\right)\mathrm{d}A, \tag{1}$$

where Γ_{face} is the set of all faces of the grain, V is the grain volume, κ_1 and κ_2 are the principle curvatures, $2\mathcal{H} = \kappa_1 + \kappa_2$ is the local mean curvature, n_i are the components of the normal along the principle coordinate directions. The exact integral for 2D grain growth was obtained by von Neumann and Mullins [4, 5] in the 1950s. In 2007, MacPherson and Srolovitz [6] derived an exact solution in 3D for an isotropic material (*i.e.*, the reduced mobility $m = M\gamma$ is identical for all grain boundaries and there is no inclination dependence of the energy, that is the second term in Eq. 1 is 0):

$$\frac{\mathrm{d}V}{\mathrm{d}t} = -2\pi m\left(\mathcal{L}_{\mathrm{grain}} - \frac{1}{6}\mathcal{M}\right). \tag{2}$$

Here $\mathcal{L}_{\mathrm{grain}}$ is the mean width of a grain [6], and $\mathcal{M}$ is the total triple-line length of the grain. Despite the elegant mathematics, to our knowledge, this relationship has not tested experimentally, and it is not clear to what extent this theory applies to grain growth in crystalline materials, which typically show anisotropy.

The lack of validation reflects a lack of experimental methods that can provide time resolved 3D measurements of grain growth, representing both a statistically relevant set of grains and the required time and spatial resolution. The development of nondestructive 3D grain mapping techniques such as three-dimensional x-ray diffraction (3DXRD) [18] and diffraction contrast tomography (DCT) [19, 20], provides a possible remedy to the situation. The first 3DXRD results on the growth of 480 Al-Mn grains by Schmidt *et al.* [21], involved six time-steps and a resolution of about $5 - 8\ \mu m$. Li [22] later used 3DXRD to measure the growth of about 2000 pure nickel grains with a slightly improved resolution. Concerning DCT, Syha [23] measured two steps of grain growth in strontium titanate sample with 849 grains and with a voxel size of $0.7\ \mu m$. Recently, Sun *et al.* [24] studied three steps of grain growth of more than 300 grains using a laboratory-based DCT [25, 26] with a voxel size of $5\ \mu m$. However, in all cases, the experimental settings were not ideal for a detailed test of

the above grain growth models. Phase contrast tomography (PCT) using decoration of the grain boundaries as a contrast is an alternative method exhibiting a superior spatial resolution [27]. However, the process is not representative of classical grain growth and PCT does not provide crystallographic information.

In this work, we present a high-resolution time resolved 3D measurements of grain growth of pure Fe, a material with anisotropic grain boundary energies [28] and mobilities [29]. Using DCT, 3D grain maps were acquired with a voxel size of 1.54 μm during annealing at 800°C for a total of 15 time-steps. The 1327 initial grains reduced to 776 in the last time-step. Based on this dataset, a comprehensive and statistically-sound analysis of crystallographic, geometrical and topological evolution during grain growth can be conducted. In this paper (part I), we present a statistical analysis of grain-based quantities, including the growth kinetics for the individual grains. To ease the discussion, the MacPherson-Srolovitz (MS) model [6] is used to rationalize our results. Local analysis of specific grain boundaries and topological analysis will be the focus of upcoming papers.

2. Methods

2.1. Experimental details

The sample material is 99.9% pure polycrystalline iron. The raw material was cold rolled to a reduction in thickness of 50% and subsequently annealed at a temperature of 700°C for 30 minutes to become fully recrystallized with an average grain radius of ∼20 μm. Cylindrical samples were cut with the rolling direction (RD) along the cylinder axis and subsequently electrochemically etched to a diameter of approximately 500 μm to remove the damage caused by the cutting.

The DCT experiment took place at beamline ID11 at the European Synchrotron Radiation Facility (ESRF) using a monochromatic x-ray beam with an energy of 40 keV. The sample was mounted on an ω rotation stage with RD parallel to the vertical rotation axis. A uniform beam illuminated the cylinder with a height of 400 μm. Both the diffracted and the transmitted beam were recorded using a near-field detector (comprising a transparent luminescent screen, with the emerging light optically coupled to a CCD) with 2048×2048 pixels and an effective pixel size of 1.54 μm. The detector was placed at ∼4.65 mm from the sample, implying that diffraction spots from individual grains from the first 5 hkl families were recorded. A continuous scan was made in ω with a range of 360°, in intervals of 0.1° and with exposure times of 1 s. Detailed information about the DCT set-up can be found in [30]. Nearly all diffraction spots were found to be distinct, appearing in one or at most two rotation step(s), indicating that the mosaic spread of all grains was below 0.2° and for most below 0.1°.

During the experiment, the sample was alternately mapped in air at room temperature and annealed on the beamline. For the annealing, a retractable tube furnace was used, operated at a constant temperature of 800°C and with a flow of a forming gas (Ar+2%H_2) to prevent sample oxidation. After annealing,

the sample was cooled by a jet of the forming gas and allowed to stabilize for 5 minutes before starting a new DCT acquisition. In total, the sample was annealed 14 times with annealing times of either ∼10 or 5 minutes (see Table 1). Notably, the time duration of the first annealing step was less accurately determined, so this time-step will be discarded when comparing with analytical models of time evolution.

The data was analyzed using a DCT analysis package at ID11 using the Networked Interactive Computing Environment (NICE) cluster [31]. The spatial resolution of the DCT reconstruction is $1-2$ voxels (*i.e.* $1.5-3$ μm), as demonstrated previously by Ludwig *et al.* [30] by comparison to PCT, and by Lenthe *et al.* [32] by comparison with TriBeam.

2.2. Determining mean width parameters

As we will use the MS model to interpret our results, relevant parameters in this model are calculated based on the DCT dataset. We define the mean width of a grain, $\mathcal{L}_{\text{grain}}$, and the mean width of the set of all faces of this grain, $\mathcal{L}_{\text{face}}$, as

$$\mathcal{L}_{\text{grain}} := \frac{1}{\pi}\int_{\partial\Omega_{\text{grain}}} \mathcal{H}\,\mathrm{d}A, \quad \mathcal{L}_{\text{face}} := \frac{1}{\pi}\int_{\Gamma_{\text{face}}} \mathcal{H}\,\mathrm{d}A,$$

where the integral over Γ_{face} does not take into account the turning angle at the triple-lines/edges while the integral over $\partial\Omega_{\text{grain}}$ does. We also define the mean width of the set of triple-lines/edges of the grain

$$\mathcal{L}_{\text{edge}} := \mathcal{L}_{\text{grain}} - \mathcal{L}_{\text{face}}. \tag{3}$$

For isotropic materials, Eq. 1 can be written as:

$$\frac{\mathrm{d}V}{\mathrm{d}t} = -2\pi m\left(\mathcal{L}_{\text{grain}} - \mathcal{L}_{\text{edge}}\right) = -2\pi m\mathcal{L}_{\text{face}}. \tag{4}$$

Comparing Eq. 4 with Eq. 2, for isotropic materials $\mathcal{L}_{\text{edge}}$ equals $\mathcal{M}/6$.

To determine the mean width parameters, the measured voxelized 3D grain volumes were firstly reconstructed into surface meshes using the multiple material marching cubes algorithm [33]. Then the mesh was smoothed using a two-step Laplacian smoothing algorithm. In Laplacian surface mesh smoothing, the location of the vertex point $\boldsymbol{v}_i$ of the surface mesh, in the $n+1$ iteration is described by:

$$\boldsymbol{v}_{i_{n+1}} = \boldsymbol{v}_{i_n} + \frac{\lambda}{C}\sum_{j=0}^{C}\left(\boldsymbol{v}_{j_n} - \boldsymbol{v}_{i_n}\right), \tag{5}$$

where λ is a scalar that describes the rate of smoothing for each iteration, $\boldsymbol{v}_j$ is the location of a vertex point j that is connected to vertex point i, and C is the number of vertex points connected to i. This then is repeated for N iterations until the desired amount of smoothing is achieved. The value of λ was chosen to keep the evolution of the mesh stable: $\lambda = 0.05$. In a two-step process, first the mesh points that describe the triple-lines and quad-points were extracted and

smoothed for $N = 200$ iterations. These smoothed triple-line points were then placed back into the surface mesh and held constant while the vertex points that constitute the grain faces were smoothed for $N = 200$ iterations. The reasoning for choosing the number of iterations and the effect of the number of smoothing iterations on the measured properties is provided in Section S1. From this smoothed surface mesh the mean width parameters $\mathcal{L}_{\text{face}}$ and $\mathcal{L}_{\text{grain}}$, as well as the total triple-line length of the grain, $\mathcal{M}$, were calculated, see [34] for details. $\mathcal{L}_{\text{edge}}$ was then calculated from Eq. 3.

2.3. Correlation between parameters

We derive relationships between the mean width parameters and two commonly used parameters: the equivalent radius R ($R = (3V/4\pi)^{1/3}$, where V is the grain volume) and the number of faces F of a grain.

For isotropic materials, according to Hillert [35], the growth of a grain with radius R follows

$$\frac{\mathrm{d}R}{\mathrm{d}t} = \alpha m \left(\frac{1}{R_{\text{cr}}} - \frac{1}{R} \right), \tag{6}$$

where R_{cr} is a critical radius and α is a geometry parameter. Substituting Eq. 6 into Eq. 2, we derive an analytical relationship between $\mathcal{L}_{\text{face}}$ and R:

$$\mathcal{L}_{\text{face}} = 2\alpha \left(R - \frac{1}{R_{\text{cr}}} R^2 \right). \tag{7}$$

Notably, $\mathcal{L}_{\text{face}}$ equals zero for $R = 0$ and $R = R_{\text{cr}}$. Next, as the mean width of grain $\mathcal{L}_{\text{grain}}$ is a linear measure of grain size, we assume a phenomenological expression:

$$\mathcal{L}_{\text{grain}} = k_1 R, \tag{8}$$

where k_1 is a dimensionless coefficient. From Eqs. 3, 7 and 8, it then follows that $\mathcal{L}_{\text{edge}}$ is a quadratic function of R.

For the correlation between R and F, we note that according to the MS theory [6], $\mathcal{L}_{\text{edge}}/\mathcal{L}_{\text{grain}}$ is proportional to the square root of F. Using Eqs. 3, 7 and 8, we have

$$\sqrt{F} = k \frac{R}{\langle R \rangle} + \sqrt{F_0}, \tag{9}$$

where k and F_0 are dimensionless constants, and $\langle R \rangle$ is the average equivalent spherical radius. We interpret F_0 as the face number of a shrinking grain just before it disappears, here named the disappearing face number. Substituting Eq. 9 into Eq. 7, and using $R_{\text{cr}} = \langle R^2 \rangle / \langle R \rangle$ [36], we have

$$\frac{\mathcal{L}_{\text{face}}}{\langle R \rangle} = -c_0 (\sqrt{F} - \sqrt{F_0})(\sqrt{F} - \sqrt{F_{\text{cr}}}), \tag{10}$$

where $c_0 = 2\alpha/k^2$, F_0, and $F_{\text{cr}} = (k + \sqrt{F_0})^2$ are dimensionless constants. This equation exhibits two zero points corresponding to the disappearing face number F_0 and the critical face number F_{cr}, respectively. A grain with face number F_{cr}

will neither grow nor shrink. Similarly, we can derive an expression between $\mathcal{L}_{\text{grain}}$ and F

$$\frac{\mathcal{L}_{\text{grain}}}{\langle R \rangle} = -c_1(\sqrt{F} - \sqrt{F_0}), \tag{11}$$

where $c_1 = k_1/k$ is a dimensionless constant.

3. Results

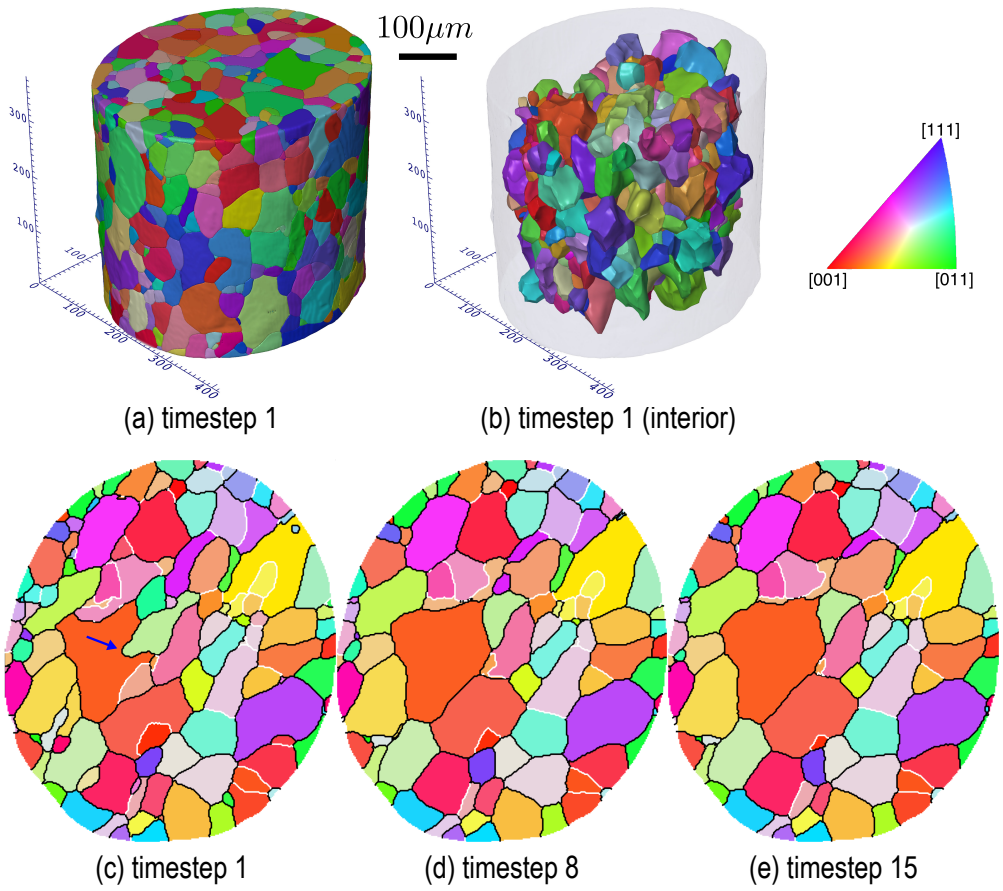

Figure 1: Experimental results. Above: 3D grain maps for time-step 1, displaying (a) all grains and (b) only interior grains. Below: one section of the 3D grain map for time-step 1 (c), 8 (d), and 15 (e). The color represents the grain orientation along sample RD (see the insert triangle), while black and white lines in (c)-(e) represent boundaries with misorientations above and below 15°, respectively.

The reconstructed 3D grain map of time-step 1 is shown in Fig. 1a. A 3D movie of the growth of one grain is given in the supplementary materials. During annealing, a significant amount of grain growth occurs, as evidenced in the evolution of one slice close to the center of the illuminated volume, cf. Fig. 1c-e.

3.1. Basic grain growth analysis

As a first step in the analysis chain, sample boundary effects were removed by discarding all "surface grains." Similar to previous work [34], this sorting of grains can be done in an unbiased way by setting two criteria:

1. grains directly touching the sample surface and surface of the top and bottom of the illuminated cylinder are removed,
2. grains whose center are within a given distance to the sample surface are removed. This distance is determined to be 46 μm, valid for all time-steps (see Section S2 in supplementary materials).

The interior grains at time-step 1 are shown in Fig. 1b. These represent less than 1/3 of the total number of grains (see Table 1). The analysis of this paper is based only on the interior grains.

Table 1: Overview of grain statistics. The average equivalent spherical radius $\langle R \rangle$ and the average number of faces $\langle F \rangle$ represent the average over interior grains.

Time-step	Time/min	Number of grains	Number of interior grains	$\langle R \rangle / \mu m$	$\langle F \rangle$
1	0	1327	387	19.30	13.49
2	10	1174	330	20.96	13.65
3	15	1069	286	22.32	13.71
4	20	1019	269	22.93	13.65
5	25	956	253	23.70	13.81
6	30	950	244	23.78	13.73
7	35	933	237	23.90	13.70
8	40	903	223	24.55	13.72
9	45	841	212	25.34	13.95
10	50	837	208	25.42	13.93
11	55	847	204	25.65	13.84
12	60	834	201	25.81	13.85
13	65	833	200	25.73	13.75
14	70	783	193	26.23	13.89
15	75	776	189	26.45	13.94

Table 1 provides statistics on basic grain parameters as a function of time: the number of total/interior grains, $\langle R \rangle$ and $\langle F \rangle$. Here R is calculated by counting the number of voxels belonging to a particular grain, while F is based on nearest neighbors.

The average number of faces is seen to be almost constant during the grain growth. Taking into account all 15 steps, the average number of faces is $\langle F \rangle = 13.77 \pm 0.13$. This value is very close to previous results from computer simulations: 13.7 [13] and 13.769 [10], and from experiment: 13.7 [34].

During the 14 annealing steps, the number of interior grains reduces by about one half. At the same time, the average radius of the grains grows about

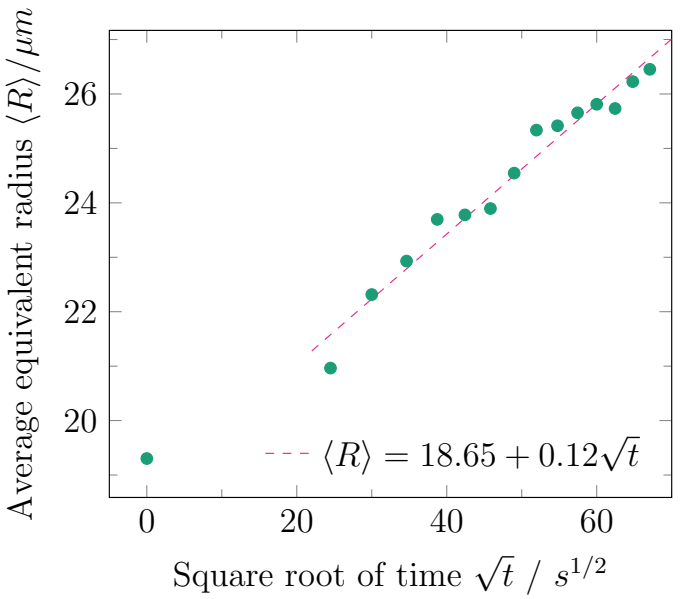

Figure 2: The average grain size $\langle R \rangle$ as a function of the square root of time $\sqrt{t}$. The dashed line shows the linear regression of the data. The first data point ($t = 0$) is not used in the fitting.

40%. This amount of growth is, however, insufficient to determine precisely the growth exponent. In Fig. 2 the average radius $\langle R \rangle$ is plotted as a function of the square root of time. Within the experimental uncertainty, the evolution of $\langle R \rangle$ is consistent with the parabolic growth. Detailed analysis of the growth will be given in Section 3.3.

3.2. Evolution in texture, geometry and topology

At the beginning of the experiment the sample has a weak texture, which is inherited from recrystallization. The texture of the sample is slightly strengthened during the annealing (see Fig. S4 in supplementary materials). The distribution of misorientation angles at time-steps 1, 8 and 15 are shown in Fig. 3. The initial distribution is relatively close to that of a sample with a random texture, except for a relatively higher fraction of low angle boundaries ($< 15°$). This is likely to be related to the texture of the sample. During the annealing, the fraction of low angle boundaries decreases by about 2.4%.

3.2.1. Distributions

The distribution of R and F, with averages listed in Table 1, are shown in Fig. 4a and 4b, respectively, for time-steps 1, 8 and 15 approximately the same change in $\langle R \rangle$ between each of the noted time-steps. The normalized grain size distribution (Fig. 4a) exhibits a peak shift from $R/\langle R \rangle = 0.6$ to 0.8 during the annealing, and the fraction of the small grains reduces markedly with time, indicating that the growth is not fully self-similar. Likewise, the distribution of

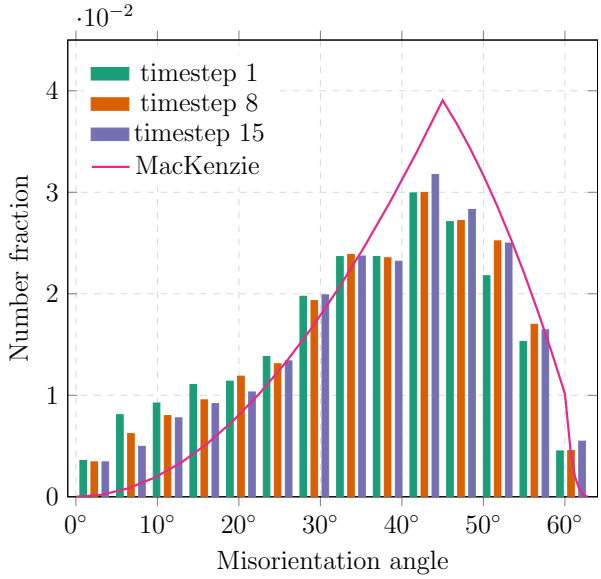

Figure 3: The misorientation distribution for three time-steps in bins of 4.5°. Overlaid is the theoretical distribution of a random texture (MacKenzie) [37].

the number of faces per grain (Fig. 4b) exhibits a peak shift, and, again, the tail of the distribution on the lower side decreases during the grain growth. This is consistent with Fig. 4a since small grains tend to have a small number of faces.

The distributions of two of the mean width parameters are shown in Fig. 4c and 4d. $\mathcal{L}_{\text{grain}}$ (Fig. 4c) is a linear measure of grain size, exhibiting a similar shape and evolution as the normalized grain size distribution in Fig. 4a. The distribution of $\mathcal{L}_{\text{face}}$ is shown in Fig. 4d. At all times, there is a peak near zero, and an asymmetric distribution with the tail of negative $\mathcal{L}_{\text{face}}$ (growing grains according to Eq. 4) much broader than that of positive $\mathcal{L}_{\text{face}}$ (shrinking grains according to Eq. 4). This is reasonable as growing grains are generally large with complex geometries, thus causing a large scatter in the values.

3.2.2. Correlation between geometrical and topological quantities

For each time-step, the mean width parameters are plotted against the grain size R to examine their correlation. As an example, the plot for time-step 8 is shown in Fig. 5. Small grains tend to have a positive $\mathcal{L}_{\text{face}}$, and vice versa. Despite some scatter, the relations proposed in Section 2.3 (Eq. 7 and Eq. 8) fit the mean width data well. The quality of fit is very similar for all 15 time-steps, and the fitted values of α and k_1 are nearly identical (see Table S1 in supplementary materials). Taking into account all 15 time-steps, on average $\alpha = 1.18 \pm 0.12$ (all errors represent standard deviations of the data in this paper). This value is similar to results from phase-field simulations ($\alpha = 1.1$ [38] and $\alpha \approx 1.25$ [39]), but slightly higher than the heuristic assumption in the Hillert theory ($\alpha = 1$) for 3D growth [35]. Theoretically, the critical radius R_{cr} is predicted to be $R_{\text{cr}}^{\text{H}} = 1.125\langle R \rangle$ by Hillert [35], and $R_{\text{cr}}^{\text{R}} = \langle R^2 \rangle / \langle R \rangle$

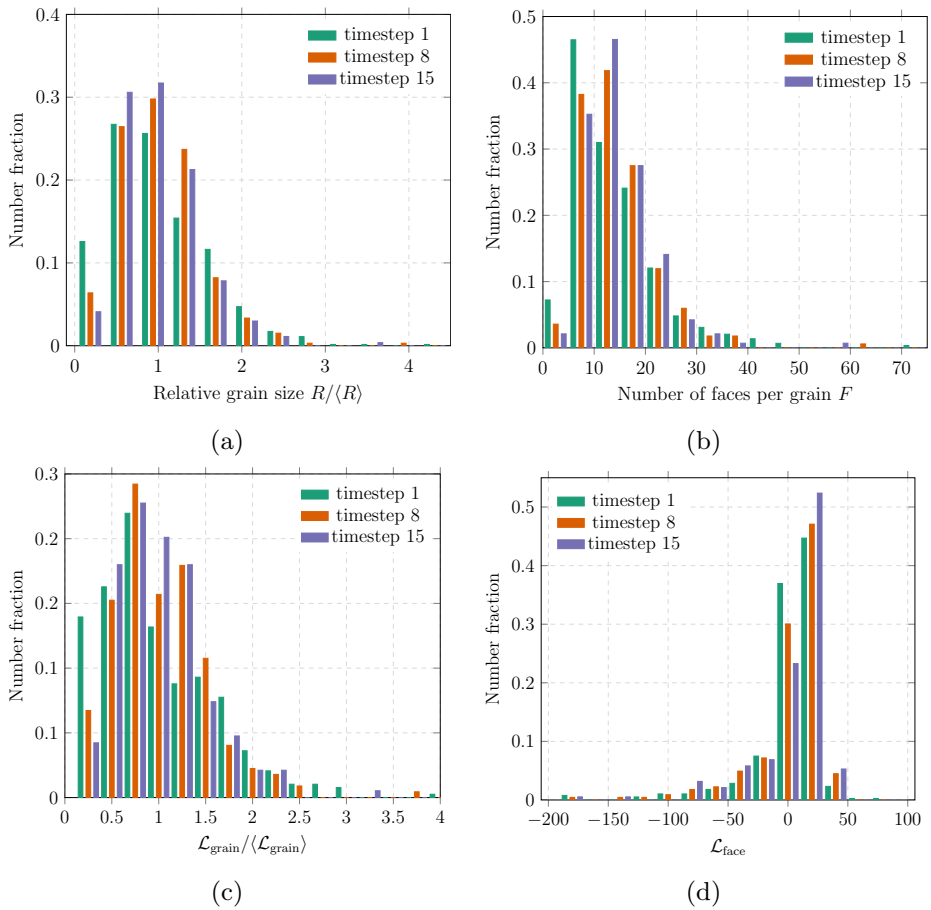

Figure 4: Distributions of four geometrical and topological parameters for three time-steps 1, 8 and 15: (a) normalized grain size $R/\langle R\rangle$, (b) number of faces per grain F, (c) normalized $\mathcal{L}_{\text{grain}}$, and (d) $\mathcal{L}_{\text{face}}$. The bins are 0.375 (a), 5 (b), 0.25 (c) and 20 (d), respectively.

by Rios [36]. Comparing to these theories, the fitted R_{cr} has a similar value: $R_{\text{cr}} = (1.12 \pm 0.05)R_{\text{cr}}^{\text{H}} = (1.04 \pm 0.02)R_{\text{cr}}^{\text{R}}$. Also evident from Fig. 5 is that a linear fit to the $\mathcal{L}_{\text{grain}}$ data and a quadratic fit to the $\mathcal{L}_{\text{edge}}$ data both show good agreement, cf. Fig. 5.

This analysis suggests a way to estimate the abstract and difficult-to-measure mean width parameters from the conventional parameter, grain size R, which is more readily available from a 3D dataset. However, the applicability of the values of the fitting parameters, *e.g.* α and $R_{\text{cr}}/\langle R\rangle$, for other materials systems has to be tested.

Then, we consider the correlation between R and F as given in Eq. 9. The data of three different time-steps are shown in Fig. 6. The dashed lines represent linear regressions of the data. Though the data display significant scatter, as a result of neglecting the underlying geometry, a linear relationship between R and $\sqrt{F}$ is in all cases seen. The fitted values of the disappearing face number

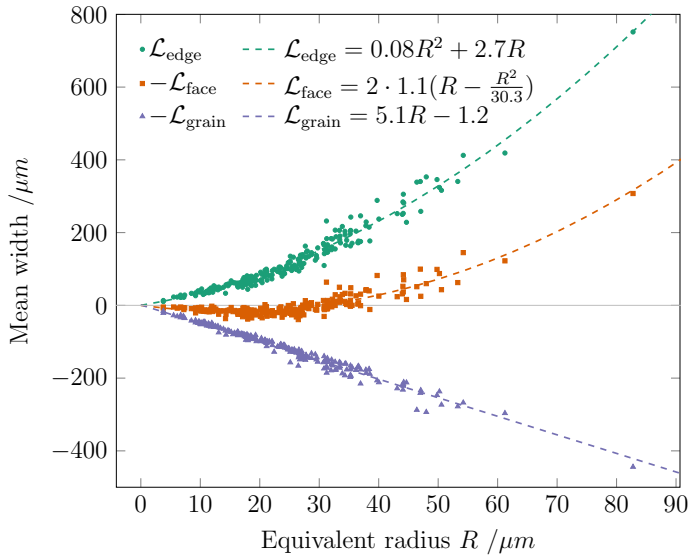

Figure 5: $\mathcal{L}_{\text{edge}}$, $-\mathcal{L}_{\text{face}}$ and $-\mathcal{L}_{\text{grain}}$ as functions of the equivalent radius R for time-step 8. The dashed lines show the results of quadratic fits to the $\mathcal{L}_{\text{face}}$ and $\mathcal{L}_{\text{edge}}$ data, and a linear fit to $\mathcal{L}_{\text{grain}}$.

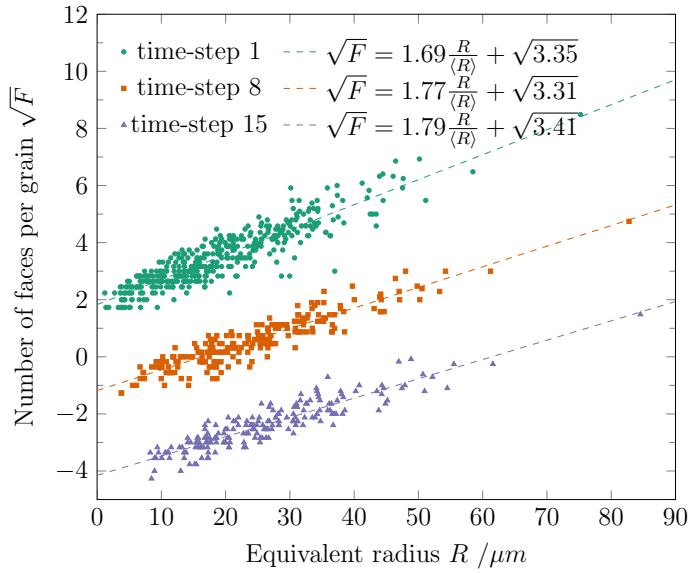

Figure 6: The equivalent radius R vs. the number of grain faces F for time-steps 1, 8 and 15. To ease visualization, the data of time-step 8 and time-step 15 are shifted downward by 3 and 6 units, respectively.

are on average $F_0 = 3.33 \pm 0.10$, which is consistent with the argument of Smith [1]: a shrinking grain has three faces before disappearing: $F_0 = 3$. The slope is nearly identical for the various time-steps: on average $k = 1.77 \pm 0.03$. The fitted

values for the 15 time-steps are listed in Table S1 in supplementary materials.

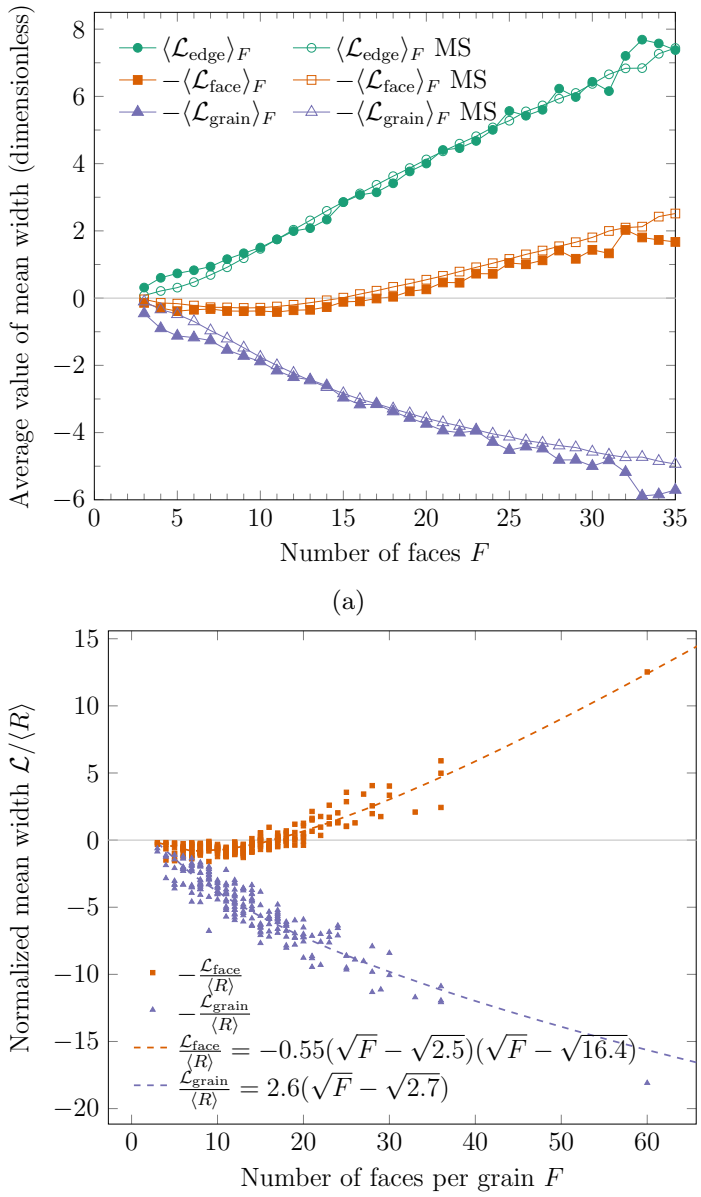

Figure 7: (a) The average values $\langle\mathcal{L}_{\text{edge}}\rangle_F$, $-\langle\mathcal{L}_{\text{face}}\rangle_F$ and $-\langle\mathcal{L}_{\text{grain}}\rangle_F$ as a function of F, using data from all 15 time-steps. Here $\langle\cdot\rangle_F$ is the topological class average (to be distinguished with the average over grain ensemble $\langle\cdot\rangle$). The measured values are scaled using $\langle V\rangle^{1/3} = 40.03\ \mu m$ (an average value representing all interior grains and all 15 time-steps). The results of a simulation based on the MacPherson-Srolovitz theory (MS) are superposed [40]. No fitting is involved in these results. (b) $-\mathcal{L}_{\text{face}}$ and $-\mathcal{L}_{\text{grain}}$ as a function of the number of grain faces F for time-step 8 (dots). Also shown are fits to analytical models (dashed lines).

Next, the correlation between mean width parameters and the number of faces is compared with simulations based on the MS theory and with the analytical expression proposed in Section 2.2.
First we consider the topological class average behavior, *i.e.* averaged for different classes of number of faces. Shown in Fig. 7a is a comparison with a MS simulation [10, 40] comprising about 200,000 grains. There is good correspondence with the simulations. Note that there are no fitting parameters in this comparison. The correspondence indicates that the topological class average mean width parameters are insensitive to the anisotropy in the grain boundary properties. Insufficient amount of data (see Fig. 7b) may cause the minor disagreement at small and large F. Moreover, errors in the mean width calculation for small grains may also contribute to the disagreement at small F as these small grains have the fewest number of voxels describing their shape, and thus the largest uncertainty in their measured morphology [41].
Then, we consider the behavior of the individual grains. As shown in Fig. 7b, fits of Eqs. 10 and 11 to the experimental data show reasonably good agreement. We attribute the scatter to anisotropy and to ignoring the underlying geometry. The fitted results of Eq. 10 are $c_0 = 0.56 \pm 0.05$, $F_0 = 2.73 \pm 0.37$ and $F_{\text{cr}} = 16.91 \pm 0.64$, and the fitted results of Eq. 11 are $c_1 = 2.58 \pm 0.11$ and $F_0 = 2.73 \pm 0.09$ (see Table S1 in supplementary materials for the fitted value of each time-step). The F_0 values are slightly smaller than the fitted values obtained in Fig. 6. The critical face number F_{cr} is slightly larger than literature values $F_{\text{cr}} = 15.5$ [34] and $F_{\text{cr}} = 15$ [40]. Notice that the fitted critical face number F_{cr} is consistent with that calculated using Eq. 9 and the critical radius R_{cr} fitted in Fig. 5.

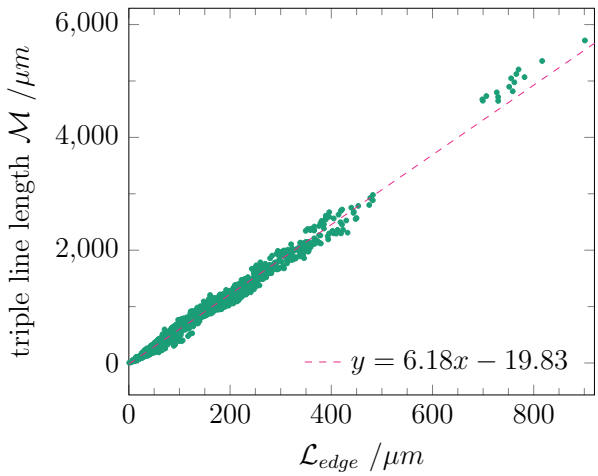

Figure 8: The total triple-line length $\mathcal{M}$ vs. $\mathcal{L}_{\text{edge}}$ (green dots) for all 15 time-steps. Overlaid is a best fit to a linear relationship.

Finally, we consider the correlation between $\mathcal{L}_{\text{edge}}$ and the total triple-line length $\mathcal{M}$. In our work, the mean width of edges $\mathcal{L}_{\text{edge}}$ is calculated from Eq. 3, so the triple-junction angle is not fixed to be the isotropic value of $2\pi/3$. In

the isotropic MS theory, $\mathcal{L}_{\text{edge}}$ is related to $\mathcal{M}$: $\mathcal{M} = 6\mathcal{L}_{\text{edge}}$. In Fig. 8, the correlation between $\mathcal{M}$ and $\mathcal{L}_{\text{edge}}$ is shown. The data are consistent with a linear relationship and a fit gives a slope of 6.16 ± 0.08. This is close to the prediction of 6 from the MS theory. As $\mathcal{M}$ and $\mathcal{L}_{\text{edge}}$ are quantities attributed to an entire grain, they may not be very sensitive to anisotropies in the individual grain boundary energies. For example, it is possible to change the grain shape significantly (as a result of grain boundary energy anisotropy) without the triple-line length $\mathcal{M}$ changing at all. Alternatively or simultaneously the anisotropy itself may be weak.

3.3. Growth rate of individual grains

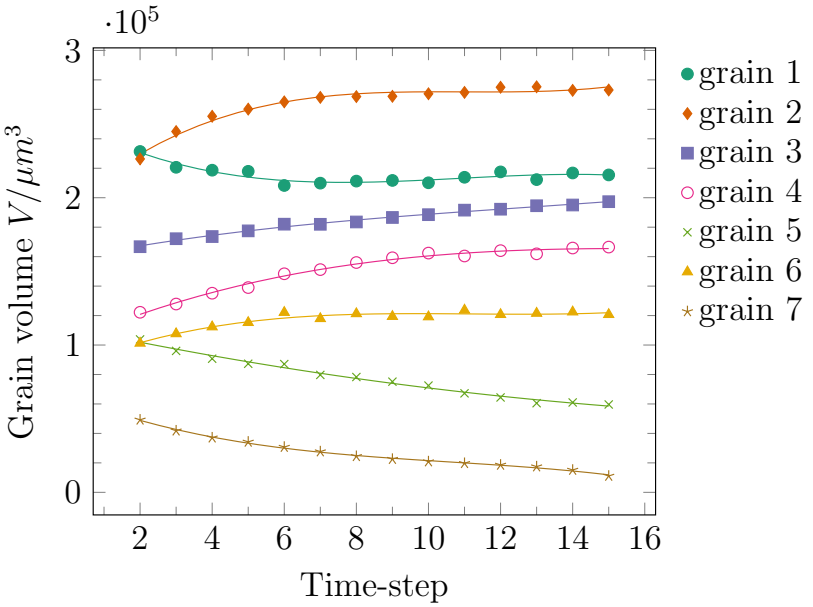

Figure 9: Examples of experimental growth curves for individual grains without (dots) and with smoothing by a third order polynomial (lines).

The growth of the individual grains were tracked through time.The evolution of the grain volume for seven randomly selected grains that survived throughout the experiment (time-step 2 to 15) are shown in Fig. 9. As illustrated, to obtain a robust measure of the growth rate $\mathrm{d}V/\mathrm{d}t$, the data are smoothed using a third-order polynomial. As one might expect, most of the large grains are growing while small grains typically are shrinking during annealing. However, there are examples of large grains that shrink (grain 1) and smaller grains that grow (grain 6), thus there is no universal value of grain volume that separates growing and shrinking grains and it is clear that whether a grain grows or shrinks depends on the local environment of the grain in contrast to the Hillert mean field theory.

The growth rates as a function of $\mathcal{L}_{\text{face}}$ is plotted for a statistically significant number of individual grains in Fig. 10a. For each time-step, despite some scatters, on average $\mathrm{d}V/\mathrm{d}t$ shows a linear correlation with $-2\pi\mathcal{L}_{\text{face}}$. Interestingly,

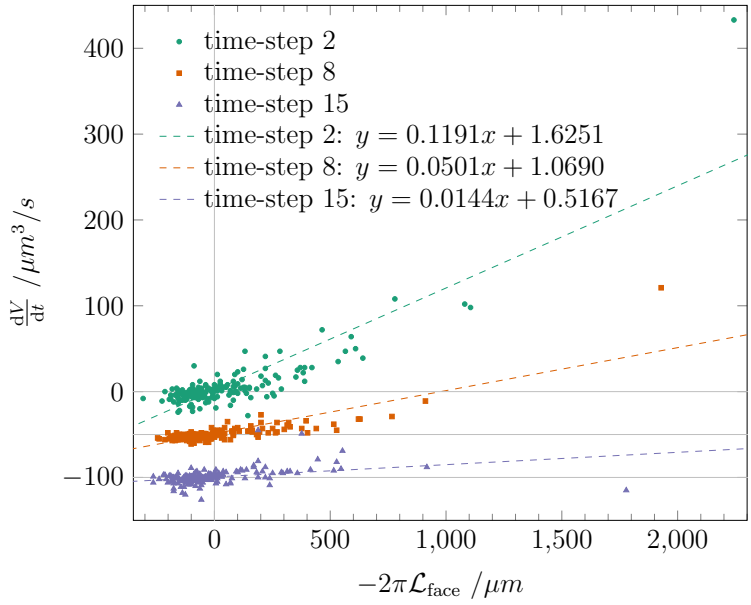

(a)

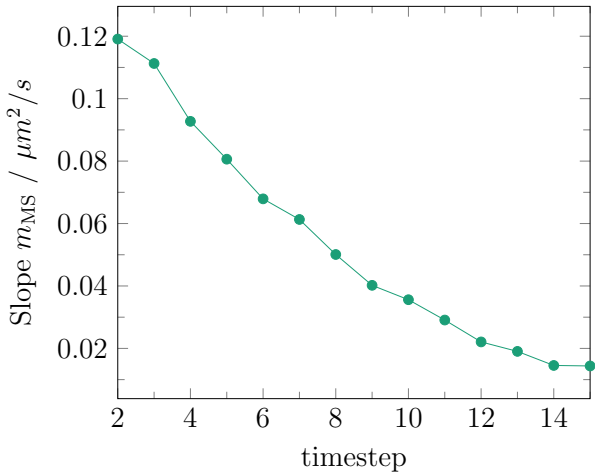

(b)

Figure 10: (a) The growth rate dV/dt is plotted versus $-\mathcal{L}_{\text{face}}$ for all grains at three time-steps. To ease visualization, the data of time-step 8 and time-step 15 have been shifted downward by 50 and 100 units, respectively. The dashed lines represent linear regressions of the data. (b) the fitted slope in (a) as a function of time.

the fitted slope ($m_{\text{MS}} = dV/dt/(-2\pi\mathcal{L}_{\text{face}})$), decreases as a function of annealing time (see Fig. 10b). Within the total annealing period, the slope decreases by a factor of 8.

4. Discussion

Over a century, a significant amount of work has been devoted to develop models that can predict the growth behavior of individual grains based on their geometry or topology, including the two outstanding models by Hillert [35], and MacPherson-Srolovitz (MS) [6] discussed above. The MS model is more elaborate as it takes into account the grain's morphology and neighbor relationships (reflected in parameter $\mathcal{L}_{\text{face}}$), while in the Hillert's model, all grains are assumed to be spheres growing in a mean field. So far none of these models have been empirically validated. The present dataset offers a unique possibility to address this issue. We can make this comparison for grain averages or by examining the results for all individual grains. Alternatively we can use the scatter in Figs. 5, 6, 7b, 8 and 10a to quantify to what extent the models are applicable on the individual grain level for anisotropic materials like iron. Below we comment and further analyze the results on first the macro scale (averaged over a grain ensembles), then the local scale (individual grains).

4.1. Macro scale grain growth

Our results in Section 3.2.2 and 3.3 demonstrate that on this scale MS theory is a good approximation for pure iron. Notably, the fitted value of the critical grain size R_{cr} from the MS model (see Fig. 5) is close to the prediction from Hillert's theory for our material. The changes in the distributions in Figs. 3 and 4 indicate that the grain growth of pure iron was not in a stationary self-similar regime during the experiment where the average grain size increases by 40 %. In particular, as shown in Fig. 4a, the shape of the grain size distribution changed. The grain size distribution is close to the log-normal distribution (see Fig. S5a in supplementary materials). During the growth, the grain size distribution becomes narrower and a peak shift is observed, c.f. Fig. S5b. The change in grain size distribution may be caused by a transition of microstructure [42] or materials anisotropy [43]. Computer simulations can be used to understand the causality of the change of distributions.

Another remarkable result on the macro scale is the fast decrease in the fitted slope m_{MS}, as shown in Fig. 10b, indicating a slowdown of grain growth. This slope decrease strongly suggests that the overall boundary characteristics have changed. From Eq. 1, the slope m_{MS} of individual grain is:

$$m_{\text{MS}} = \frac{\mathrm{d}V/\mathrm{d}t}{-2\pi\mathcal{L}_{\text{face}}} = \frac{\displaystyle\int_{\Gamma_{\text{face}}} M\gamma(\kappa_1+\kappa_2)\,\mathrm{d}A}{\displaystyle\int_{\Gamma_{\text{face}}} (\kappa_1+\kappa_2)\,\mathrm{d}A} + \frac{\displaystyle\int_{\Gamma_{\text{face}}} M\left(\frac{\partial^2\gamma}{\partial n_1^2}\kappa_1 + \frac{\partial^2\gamma}{\partial n_2^2}\kappa_2\right)\mathrm{d}A}{\displaystyle\int_{\Gamma_{\text{face}}} (\kappa_1+\kappa_2)\,\mathrm{d}A}. \tag{12}$$

Notice that for the isotropic case, the reduced grain boundary mobility, $m_{\text{MS}} = M\gamma$, must be a constant for all grains and independent of time. For anisotropic materials, both terms in Eq. 12 can change during grain growth and affect the slope m_{MS}. In the following, we discuss potential causes for the observed decrease of slope m_{MS}.

1. A decrease in the population frequency of certain grain boundaries with very high mobilities M, up to $10^3 - 10^4$ higher than low mobility ones [2, 44]. We also emphasize that the fraction of high angle boundaries *increases* (see Fig. 3), which is surprising given the fact that high angle boundaries are generally believed to have higher mobilities and energies than low angle boundaries [45]. A detailed characterization of the changes in boundary characteristics will be conducted in an upcoming paper.
2. Molecular dynamics simulations have shown that during grain growth, the boundary roughness at the atomic scale can reduce, therefore causing a decrease in boundary mobility M [46]. At the same time, local atomic scale elastic strains have recently been suggested to be a reason for a slowdown of grain growth [47]. However, to verify these mechanisms, 3D grain growth studies with atomic resolution is required, which is not possible in the near future.
3. The material contains a small amount of Mn and Ni. It is known that the solute tends to segregate at the grain boundaries during annealing [45, 48]. As the boundaries migrate, the solute accumulates, which in turn reduces the boundary mobilities [49]. To quantify this effect, some chemical analysis on individual grains boundaries using, *e.g.* atom probe [50], are required.
4. A decrease in the population of grain boundaries with large grain boundary energies γ. However is unlikely to cause the strong decrease in the slope m_{MS}, as the energies of different high angle boundaries at most vary by a factor of 2-3 [28]. Likewise, it is very unlikely that the fraction of special boundaries with significantly low energy (*e.g.* twin boundaries) increases during growth in iron [28].
5. The starting microstructure comprises some large grains with large concave retrusions at the boundaries, see the boundary marked by the blue arrow in Fig. 1c. These features are presumably inherited from recrystallization process; although significant grain growth has already occurred prior to the current experiments (the average grain radius after recrystallization is about 12 μm). These features typically lead to fast boundary migration, and the fraction of such features decreases during grain growth. As can be seen in Eq. 12, the change in curvature may lead to a change in m_{MS}. As mentioned above, a detailed characterization of the changes in boundary characteristics will be conducted in an upcoming paper.

Although the specific reason for the decrease in the fitted slope m_{MS} is not clarified, we speculate that this decrease is a general phenomenon, which is applicable to many engineering materials that contain a certain amount of impurities and with anisotropic material properties. Moreover, as the possible causes for the lack of self-similarity and the decresing slope is similar, there can be a connection between two.

4.2. Local scale grain growth

Considering now the validity of the MS model for the individual grains, we test the MS prediction that grains with a positive $\mathcal{L}_{\mathrm{face}}$ shrinks and those with

a negative $\mathcal{L}_{\text{face}}$ grows. Based on the data represented in Fig. 10a, we find that the majority ($> 70\%$) of the grains fulfill this criterion for all annealing steps. Next, we test the quantitative prediction of the growth rate $\mathrm{d}V/\mathrm{d}t$ based on $\mathcal{L}_{\text{face}}$. If the grain properties are isotropic, all the data of Fig. 10a should be on a straight line with a slope equal to the reduced mobility. The scatter in the values of the growth rates indicates that Eq. 4 does not predict the experimentally measured grain growth rates. The slopes m_{MS} from individual grains show a broad distribution (see Fig. S6) with the majority of the data concentrated around the fitted m_{MS}. This broad distribution may be partly caused by small measurement error in $\mathcal{L}_{\text{face}}$ when $\mathcal{L}_{\text{face}}$ is around zero. However, only 13% of the grains have m_{MS} within a range $\pm 25\%$ of the fitted m_{MS}. This implies that even on the grain scale where boundary properties are averaged over the number of faces F, the behavior is quite anisotropic.

Comparing different annealing times, the applicability of the model is even worse, as evidenced by the significant decrease in the slope of the linear fit as grain growth proceeds. As the slowdown from a decreasing curvature driving force is already considered in the model, this decrease in the slope arises from other mechanisms, of which candidates were presented in Section 4.1. These mechanisms are rather generic and will apply to many other polycrystalline materials. Therefore, at a certain stage of grain growth, it is a challenging task to predict how much a given grain will grow or shrink, based solely on $\mathcal{L}_{\text{face}}$ and the MS model, even with 50% uncertainty. This difficulty is mainly related to the fact that different boundaries around the same grains move differently, even taken the curvature into account. For example, some boundaries did not move much during the whole annealing period, while other boundaries move more than 30 μm. To better predict the growth rates of individual grains, the mobilities and energies for the individual boundaries have to be taken into account, as given in Eq. 1. This is the topic of a subsequent paper.

5. Conclusion

In this work, we demonstrate that DCT can provide 3D time-series of sufficient quality for advancing our current understandings of grain growth and for comprehensive tests of grain growth models. Several conclusions can be drawn based on the quantitative analysis:

- The grain growth of the iron material studied is not self-similar during the monitored interval in time and temperature. The distributions of normalized grain size, number of faces per grain, and mean width parameters exhibit shape changes during the annealing. The starting weak texture has slightly strengthened after the final annealing step, while the fraction of the low angle boundaries ($< 15°$) decreases by about 2.4%.

- Within the framework of isotropic materials, analytical expressions correlating the mean width parameters, the grain size and the number of faces are derived and validated based on the 3D dataset at individual time-steps. The results show that when averaging over the grain ensemble -

and within short time intervals - these analytical expressions describe the experimental data well.

- The growth rates for the individual grains are determined. Evidence is provided for an overall slowdown of the growth, associated with a decrease of the slope m_{MS} by a factor of 8. Several possible reasons for this decrease are discussed.

- Based on the correlation between $\mathcal{L}_{\mathrm{face}}$ and growth rate, the MacPherson-Srolovitz model correctly predicts whether a grain grows or shrinks for $> 70\%$ (range between 70% and 85% for 15 time-steps) of the grains. However, it fails to predict the exact growth rate. This is not surprising as the MS model is based on an isotropic assumption while iron is known to be anisotropic. To accurately predict the growth behavior of individual grains, Eq. 1 needs to be calculated either analytically or numerically. This requires the determination of the anisotropic grain boundary mobilities and energies.

Acknowledgments

JZ and HFP acknowledge funding from the CINEMA alliance. ESRF is acknowledged for beamtime, and the instrument center Danscatt for travel refund. JZ and YZ thank Mr. Lars Lorentzen at DTU Wind Energy for help with preparation of the sample. DJR acknowledges funding from the Office of Naval Research (ONR) under their Structural Materials Program.

References

[1] C. S. Smith, Grain shapes and other metallurgical applications of topology, Metallography, Microstructure, and Analysis 4 (1952) 543–567.

[2] G. Gottstein, L. S. Shvindlerman, Grain boundary migration in metals: thermodynamics, kinetics, applications, CRC press, 2009.

[3] G. S. Rohrer, Grain boundary energy anisotropy: a review, J. Mater. Sci. 46 (2011) 5881.

[4] J. von Neumann, Discussion: Shape of metal grains metal interfaces, American Society for Metals (1952).

[5] W. W. Mullins, Two-dimensional motion of idealized grain boundaries, J. Appl. Phys. 27 (1956) 900–904.

[6] R. D. MacPherson, D. J. Srolovitz, The von Neumann relation generalized to coarsening of three-dimensional microstructures, Nature 446 (2007) 1053–1055.

[7] T. Le, Q. Du, A generalization of the three-dimensional MacPherson-Srolovitz formula, Communications in Mathematical Sciences 7 (2009) 511–520.

[8] D. Zöllner, P. Streitenberger, Three-dimensional normal grain growth: Monte Carlo Potts model simulation and analytical mean field theory, Scr. Mater. 54 (2006) 1697–1702.

[9] M. Syha, D. Weygand, A generalized vertex dynamics model for grain growth in three dimensions, Modell. Simul. Mater. Sci. Eng. 18 (2010) 015010.

[10] E. A. Lazar, J. K. Mason, R. D. MacPherson, D. J. Srolovitz, A more accurate three-dimensional grain growth algorithm, Acta Mater. 59 (2011) 6837 – 6847.

[11] H.-K. Zhao, T. Chan, B. Merriman, S. Osher, A variational level set approach to multiphase motion, J. Comput. Phys. 127 (1996) 179–195.

[12] C. Mießen, M. Liesenjohann, L. Barrales-Mora, L. Shvindlerman, G. Gottstein, An advanced level set approach to grain growth - accounting for grain boundary anisotropy and finite triple junction mobility, Acta Mater. 99 (2015) 39 – 48.

[13] C. E. Krill III, L.-Q. Chen, Computer simulation of 3-d grain growth using a phase-field model, Acta Mater. 50 (2002) 3059–3075.

[14] N. Moelans, B. Blanpain, P. Wollants, Quantitative analysis of grain boundary properties in a generalized phase field model for grain growth in anisotropic systems, Phys. Rev. B 78 (2008) 024113.

[15] H.-K. Kim, S. G. Kim, W. Dong, I. Steinbach, B.-J. Lee, Phase-field modeling for 3d grain growth based on a grain boundary energy database, Modell. Simul. Mater. Sci. Eng. 22 (2014) 034004.

[16] G. I. Tóth, T. Pusztai, L. Gránásy, Consistent multiphase-field theory for interface driven multidomain dynamics, Phys. Rev. B 92 (2015) 184105.

[17] C. Herring, Surface tension as a motivation for sintering, in: J. M. Ball, D. Kinderlehrer, P. Podio-Guidugli, M. Slemrod (Eds.), Fundamental Contributions to the Continuum Theory of Evolving Phase Interfaces in Solids: A Collection of Reprints of 14 Seminal Papers, Springer Berlin Heidelberg, Berlin, Heidelberg, 1951, pp. 33–69. doi:10.1007/978-3-642-59938-5_2.

[18] H. F. Poulsen, Three-dimensional X-ray diffraction microscopy: mapping polycrystals and their dynamics, volume 205 of *Springer Tracts in Modern Physics*, Springer Berlin Heidelberg, 2004. doi:10.1007/b97884.

[19] W. Ludwig, S. Schmidt, E. M. Lauridsen, H. F. Poulsen, X-ray diffraction contrast tomography: a novel technique for three-dimensional grain mapping of polycrystals. I. direct beam case, J. Appl. Crystallogr. 41 (2008) 302–309.

[20] G. Johnson, A. King, M. G. Honnicke, J. Marrow, W. Ludwig, X-ray diffraction contrast tomography: a novel technique for three-dimensional grain mapping of polycrystals. ii. the combined case, J. Appl. Crystallogr. 41 (2008) 310–318.

[21] S. Schmidt, U. L. Olsen, H. F. Poulsen, H. O. Sørensen, E. M. Lauridsen, L. Margulies, C. Maurice, D. J. Jensen, Direct observation of 3-d grain growth in Al-0.1%Mn, Scr. Mater. 59 (2008) 491 – 494.

[22] S. F. F. Li, Imaging of Orientation and Geometry in Microstructures: Development and Applications of High Energy X-ray Diffraction Microscopy, Dissertation, Carnegie Mellon University, 2011. URL: `http://repository.cmu.edu/dissertations/59`.

[23] M. Syha, Microstructure evolution in strontium titanate Investigated by means of grain growth simulations and x-ray diffraction contrast tomography experiments, Ph.D. thesis, Karlsruhe Institute of Technology, 2014. URL: `https://publikationen.bibliothek.kit.edu/1000042175`. doi:`10.5445/KSP/1000042175`.

[24] J. Sun, A. Lyckegaard, Y. Zhang, S. Catherine, B. Patterson, F. Bachmann, N. Gueninchault, H. Bale, C. Holzner, E. Lauridsen, et al., 4D study of grain growth in Armco iron using laboratory x-ray diffraction contrast tomography, IOP Conference Series: Materials Science and Engineering 219 (2017) 012039.

[25] A. King, P. Reischig, J. Adrien, W. Ludwig, First laboratory X-ray diffraction contrast tomography for grain mapping of polycrystals, J. Appl. Crystallogr. 46 (2013) 1734–1740.

[26] S. McDonald, P. Reischig, C. Holzner, E. Lauridsen, P. Withers, A. Merkle, M. Feser, Non-destructive mapping of grain orientations in 3d by laboratory x-ray microscopy, Sci. Rep. 5 (2015) 14665.

[27] I. M. McKenna, S. O. Poulsen, E. M. Lauridsen, W. Ludwig, P. W. Voorhees, Grain growth in four dimensions: A comparison between simulation and experiment, Acta Mater. 78 (2014) 125–134.

[28] S. Ratanaphan, D. L. Olmsted, V. V. Bulatov, E. A. Holm, A. D. Rollett, G. S. Rohrer, Grain boundary energies in body-centered cubic metals, Acta Mater. 88 (2015) 346 – 354.

[29] Z. Zhang, Y. Zhang, O. V. Mishin, N. Tao, W. Pantleon, D. J. Jensen, Microstructural analysis of orientation-dependent recovery and recrystallization in a modified 9Cr-1Mo steel deformed by compression at a high

strain rate, Metallurgical and Materials Transactions A 47 (2016) 4682–4693.

[30] W. Ludwig, P. Reischig, A. King, M. Herbig, E. M. Lauridsen, G. Johnson, T. J. Marrow, J. Y. Buffire, Three-dimensional grain mapping by x-ray diffraction contrast tomography and the use of Friedel pairs in diffraction data analysis, Rev. Sci. Instrum. 80 (2009).

[31] P. Reischig, A. King, L. Nervo, N. Viganó, Y. Guilhem, W. J. Palenstijn, K. J. Batenburg, M. Preuss, W. Ludwig, Advances in x-ray diffraction contrast tomography: flexibility in the setup geometry and application to multiphase materials, J. Appl. Crystallogr. 46 (2013) 297–311.

[32] W. C. Lenthe, M. P. Echlin, A. Trenkle, M. Syha, P. Gumbsch, T. M. Pollock, Quantitative voxel-to-voxel comparison of TriBeam and DCT strontium titanate three-dimensional data sets, J. Appl. Crystallogr. 48 (2015) 1034–1046.

[33] Z. Wu, J. M. Sullivan, Multiple material marching cubes algorithm, Int. J. Numer. Methods Eng. 58 (2003) 189–207.

[34] D. Rowenhorst, A. Lewis, G. Spanos, Three-dimensional analysis of grain topology and interface curvature in a β-titanium alloy, Acta Mater. 58 (2010) 5511 – 5519.

[35] M. Hillert, On the theory of normal and abnormal grain growth, Acta Metall. 13 (1965) 227 – 238.

[36] P. Rios, Comparison between a computer simulated and an analytical grain size distribution, Scr. Mater. 40 (1999) 665–668.

[37] J. Mackenzie, Second paper on statistics associated with the random disorientation of cubes, Biometrika 45 (1958) 229–240.

[38] Y. Suwa, Y. Saito, H. Onodera, Parallel computer simulation of three-dimensional grain growth using the multi-phase-field model, Mater. Trans. 49 (2008) 704–709.

[39] R. D. Kamachali, I. Steinbach, 3-d phase-field simulation of grain growth: topological analysis versus mean-field approximations, Acta Mater. 60 (2012) 2719–2728.

[40] E. A. Lazar, The evolution of cellular structures via curvature flow, Ph.D. thesis, Princeton University, Applied and Computational Mathematics Department, 2011. URL: `http://arks.princeton.edu/ark:/88435/dsp01sx61dm30d`, advisor: MacPherson, Robert D; Srolovitz, David J.

[41] X. Zhong, D. J. Rowenhorst, H. Beladi, G. S. Rohrer, The five-parameter grain boundary curvature distribution in an austenitic and ferritic steel, Acta Mater. 123 (2017) 136–145.

[42] P. Rios, T. Dalpian, V. Brandao, J. Castro, A. Oliveira, Comparison of analytical grain size distributions with three-dimensional computer simulations and experimental data, Scr. Mater. 54 (2006) 1633–1637.

[43] W. Mullins, Grain growth of uniform boundaries with scaling, Acta Mater. 46 (1998) 6219–6226.

[44] D. L. Olmsted, E. A. Holm, S. M. Foiles, Survey of computed grain boundary properties in face-centered cubic metals ii: Grain boundary mobility, Acta Mater. 57 (2009) 3704 – 3713.

[45] A. Rollett, F. Humphreys, G. S. Rohrer, M. Hatherly, Recrystallization and related annealing phenomena, Elsevier, 2004.

[46] E. A. Holm, S. M. Foiles, How grain growth stops: a mechanism for grain-growth stagnation in pure materials, Science 328 (2010) 1138–1141.

[47] S. L. Thomas, K. Chen, J. Han, P. K. Purohit, D. J. Srolovitz, Reconciling grain growth and shear-coupled grain boundary migration, Nat. Commun. 8 (2017) 1764.

[48] A. Rollett, G. Gottstein, L. Shvindlerman, D. Molodov, Grain boundary mobility–a brief review, Zeitschrift für Metallkunde 95 (2004) 226–229.

[49] M. Mendelev, D. Srolovitz, Impurity effects on grain boundary migration, Modell. Simul. Mater. Sci. Eng. 10 (2002) R79.

[50] M. Herbig, D. Raabe, Y. J. Li, P. Choi, S. Zaefferer, S. Goto, Atomic-scale quantification of grain boundary segregation in nanocrystalline material, Phys. Rev. Lett. 112 (2014) 126103.

Supplementary materials

S1. Smoothing in the surface mesh reconstruction

Analyzing the geometry of the interface of data described by discrete voxels can be problematic. Using the original voxel edges will grossly overestimate the surface areas and local curvatures, thus surface smoothing methods are employed. However, there is no clear threshold for when there has been too much or too little smoothing applied. It is assumed that the grain interfaces, at these length scales, are described by smooth continuous surfaces, thus the high curvature, stair-step like artifacts of the voxel edges should be removed. But using Laplacian smoothing, it is clear that with infinite numbers of iterations, the grain faces will eventually remove all long-range curvature as well. In this section, the effect on various geometrical measurements as a function of the amount of Laplacian smoothing is considered. As outlined in Section 2.2, a two-step smoothing process is implemented, first independently smoothing the triple-lines in the mesh, then constraining the smoothed triple-lines and smoothing the grain faces. In both steps, a value of $\lambda = 0.05$ is used, and the number of smoothing iterations, N is varied. Here, only the surface mesh of the first time-step is considered, as it has the fewest number of voxels per grain on average, and thus should be the most sensitive to the surface-smoothing process. We also introduce the smoothing metric f_{vox} which is defined as the fraction of surface mesh vertex points that have moved more than the distance of a voxel dimension from the original position. In an ideal surface mesh construction, the smooth interface points should remain within the voxel that they originated within. However, it is expected that with experimental data, not all voxels, and thus not all surface mesh points will be properly labeled, and thus it is reasonable that some fraction of the surface mesh points travel further than a voxel distance from its original position.

The values of f_{vox}, average value of the spherical equivalent radius $\langle R \rangle$, average surface area per grain $\langle S_A \rangle$, average triple-line length per grain L_{TL}, the average mean width of the grain faces $\langle \mathcal{L}_{\mathrm{face}} \rangle$ and mean width of the triple-lines $\langle \mathcal{L}_{\mathrm{TL}} \rangle$ were evaluated for $N = 0, 50, 100, 150, 200, 250, 300, 500, 1000$, and the results are plotted in Fig. S1. Fig S1a shows that f_{vox}, continuously increases, although at a slower rate with increasing iterations. The rate of change of the average radius shown in Fig S1b shows an overall decrease in the average radius with iteration, but note that the total change in the mean grain size is 0.01% for $N = 1000$, a negligible change.

The average surface area of the grains as a function of smoothing iteration, Fig. S1c shows the more characteristic behavior, initially with no smoothing the value of the surface area is very high and even moderate amount of smoothing leads to a dramatic reduction in the value. But as smoothing continues, the reduction in the surface area slows. The inset graph shows that the variation in $\langle S_A \rangle$from $N = 100$ to $N = 300$ is only 0.9%. The values of $\langle L_{\mathrm{TL}} \rangle$ and $\langle \mathcal{L}_{\mathrm{TL}} \rangle$ shown in Fig. S1d and e, show a similar trend although the values continue to see a decrease in value with more iterations, but still at a slower rate than the initial changes from no smoothing. This is most likely because in the two-step

smoothing nothing constrains the triple-lines during the smoothing, thus in the limit of very high iterations the triple-lines would remove all curvatures and assume straight lines between the quad-points. Nonetheless, the total variation in the measurement of $\langle L_{\mathrm{TL}} \rangle$ and $\langle \mathcal{L}_{\mathrm{TL}} \rangle$ between $N = 100$ to 300 is 3% and 6% respectively. The higher variation for $\langle \mathcal{L}_{\mathrm{TL}} \rangle$ is not surprising, given that the variation in length, and line curvature are both represented here.

Fig. S1f shows the change in the average mean width of the grain faces, which shows the initial reduction in value which is directly related to the reduction in surface area. The value passes through a minima near $N = 150 - 200$, then it slowly starts increasing again. It is not immediately clear what causes this increase, since the surface area is relatively constant over the domain of $N > 150$. Since most of the measured mesh is conformal, a reduction in the negative curvature in one grain would be matched by the reduction in curvature of the positive curvature in the neighboring grain. Thus this increase in the curvature must be related to interfaces that would be contacting the outside touching grains which are not included in the average. Thus we have chosen that $N = 200$ provides the best compromise of reducing the number of artifacts from the original voxel faces, while not reducing the long-range curvature of the grain boundaries.

S2. Convergence study of unbiased selection

As most grain growth theories assume that grains grow in an infinite medium, grains close to the free surface should not be used in the analysis to compare with these theories. Grains whose center are within a given distance to the free surface are removed. The distance is found by a convergence study of time-steps 1 and 15 to ensure average grain size $\langle R \rangle$ and average face number $\langle F \rangle$ of the interior grains reach a stable value, see Fig. S2. The convergence is seen to be achieved around 30 voxels, equivalent to about 46 μm. This value is applied to all time-steps to remove surface grains.

S3. Reproducibility of the DCT scan

In order to estimate spatial resolution and test reproducibility, the last time-step was repeated with slightly different experimental parameters: the sample was translated upward by 5 μm and the detector to sample distance was increased by 10 μm. The result is shown in Fig. S3. The average shift in position is 0.305 voxels, corresponding to $0.47 \mu m$.

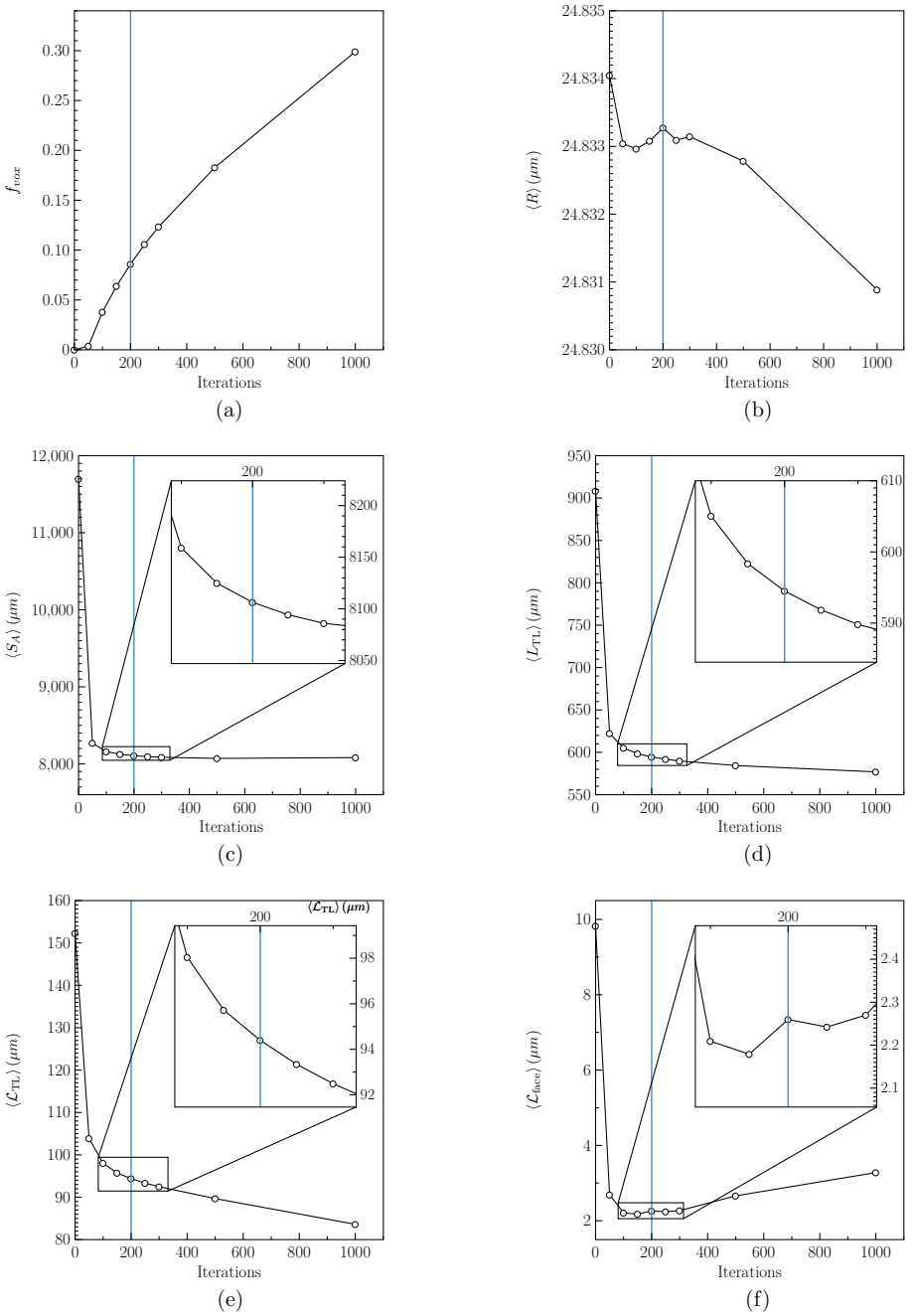

Figure S1: Effect of the extent of smoothing on the measurement of geometry parameters.

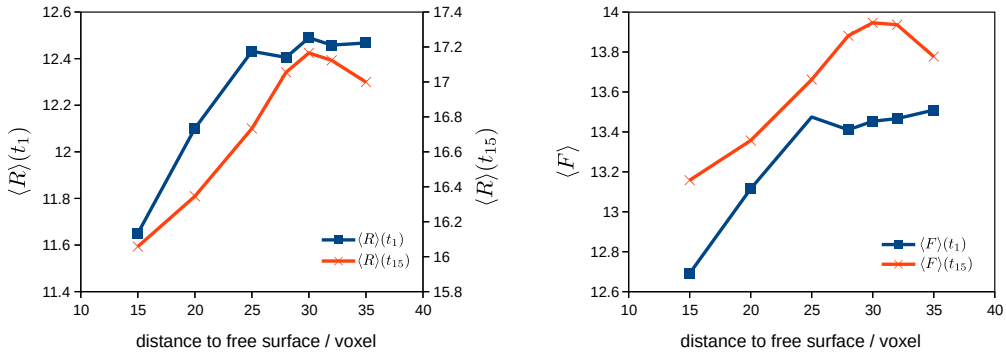

Figure S2: Unbiased selection: convergence of average radius $\langle R\rangle$ and average face number $\langle F\rangle$ calculated using interior grains as a function of distance to the free surface.

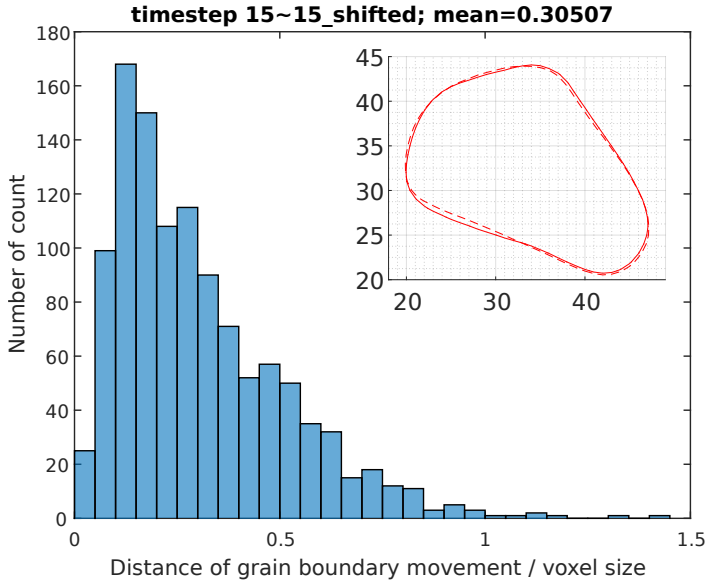

Figure S3: Test of reproducibility. A histogram is provided of the difference in position of the reconstructed grain boundary between two scans with minor changes in detector position. An example of the change in morphology of one grain boundary is shown in the insert with units of μm. The solid line represents the grain morphology of time-step 15 and the dashed line the additional scan.

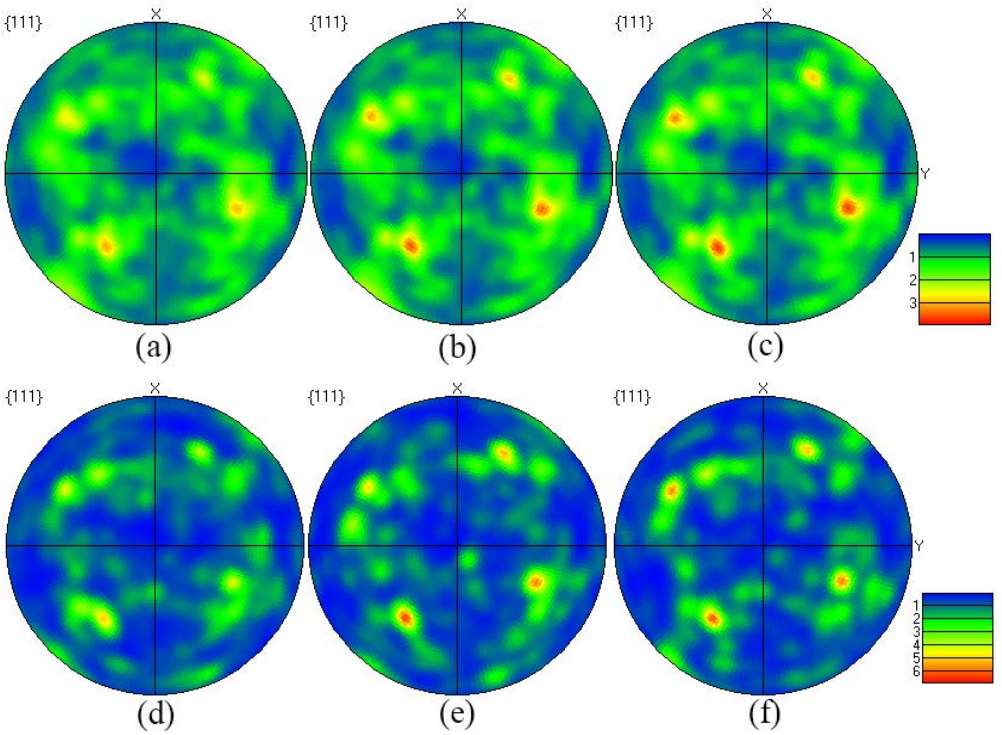

Figure S4: Texture of all and the interior grains in the gauge volume. (a)-(c) for the whole sample volume at time-steps 1, 8 and 15; (d)-(f) for interior grains at time-steps 1, 8 and 15. The texture of the whole gauge volume strengthens slightly during annealing, while the texture of the interior grains strengthens first and then weakens afterward. Notice that the statistics for interior grains are relatively poor, especially in the late stage of the growth.

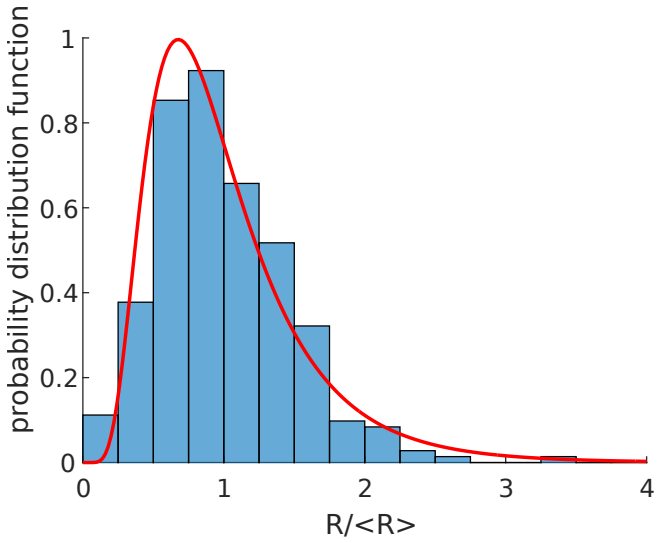

(a)

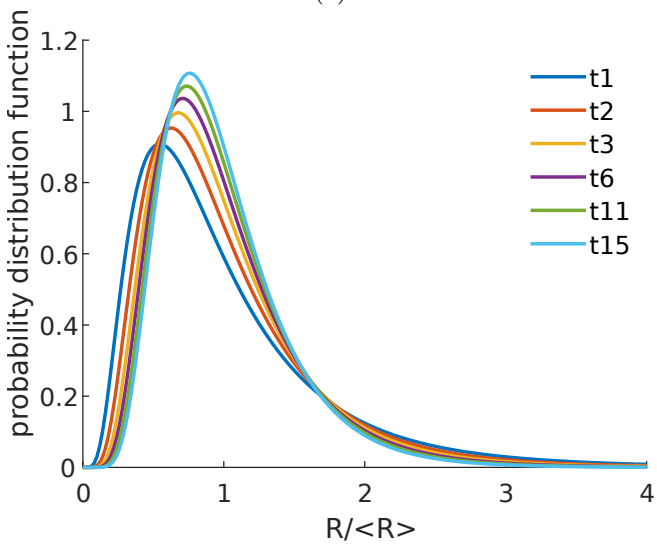

(b)

Figure S5: Log-normal fit of the grain size distribution. (a) is the log-normal fit of time-step 3. (b) is the change of fitted log-normal distributions with time. Notice here the probability distribution function differs from the number fraction used in Fig. 4a by a constant scale.

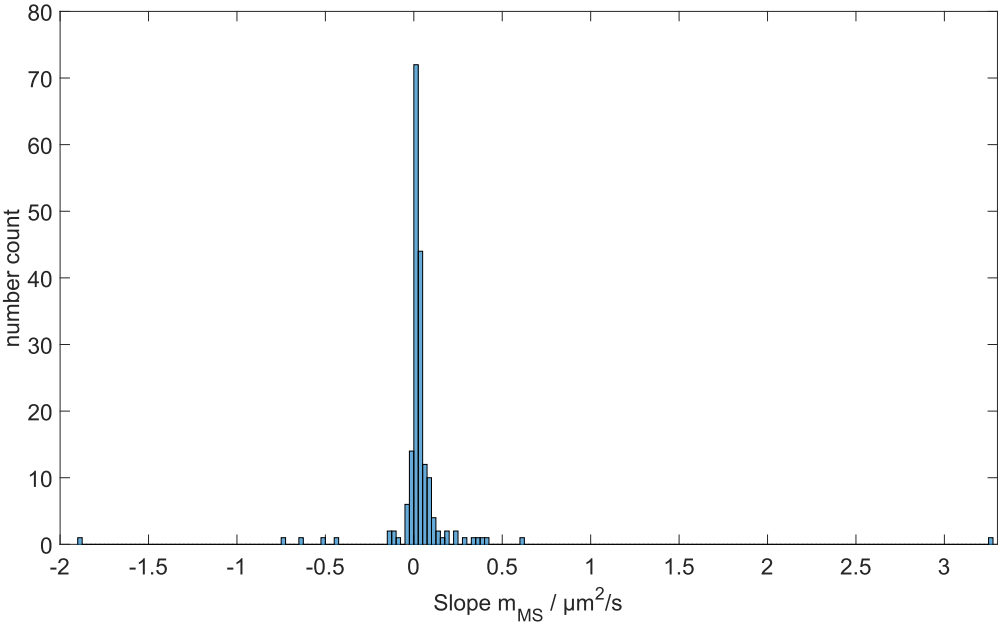

Figure S6: The distribution of the apparent reduced mobilities calculated from individual grains for time-step 8. Bin size is 0.025 $\mu m^2/s$.

Table S1: List of fitted values of parameters in Section 2.3 for each time-step

Time-step	Eq. 7		Eq. 8	Eq. 9		Eq. 10			Eq. 11	
	α	R_{cr}	k_1	k	F_0	c_0	F_0	F_{cr}	c_1	F_0
1	1.41	27.15	5.77	1.69	3.35	0.66	3.57	18.55	2.88	2.93
2	1.35	27.94	5.60	1.76	3.23	0.62	3.30	17.88	2.70	2.73
3	1.24	28.73	5.52	1.79	3.20	0.55	2.88	17.33	2.61	2.67
4	1.28	29.54	5.47	1.80	3.15	0.58	2.67	17.11	2.60	2.64
5	1.25	29.96	5.42	1.82	3.19	0.57	2.81	16.98	2.55	2.66
6	1.24	30.11	5.28	1.76	3.35	0.58	2.83	16.83	2.61	2.84
7	1.16	30.65	5.18	1.75	3.36	0.58	2.97	17.16	2.62	2.83
8	1.10	30.27	5.10	1.77	3.31	0.55	2.51	16.44	2.57	2.74
9	1.21	31.62	5.31	1.80	3.38	0.58	2.80	16.89	2.54	2.79
10	1.03	31.14	5.10	1.79	3.39	0.49	2.30	16.46	2.51	2.74
11	1.03	31.33	5.08	1.78	3.38	0.49	2.24	16.25	2.49	2.68
12	1.08	31.65	5.13	1.77	3.43	0.53	2.59	16.36	2.50	2.71
13	0.99	31.26	5.00	1.78	3.33	0.51	2.45	16.34	2.49	2.62
14	1.17	32.57	5.23	1.77	3.47	0.56	2.71	16.70	2.51	2.73
15	1.11	32.37	5.18	1.79	3.41	0.51	2.26	16.33	2.45	2.64